This is a repository copy of *A high-performance primary nanosheet heterojunction cathode composed of Na0.44MnO2 tunnels and layered Na2Mn3O7 for Na-ion batteries*.

White Rose Research Online URL for this paper:
http://eprints.whiterose.ac.uk/161430/

Version: Accepted Version

Article:
Zheng, P., Su, J., Wang, Y. et al. (5 more authors) (2020) A high-performance primary nanosheet heterojunction cathode composed of Na0.44MnO2 tunnels and layered Na2Mn3O7 for Na-ion batteries. ChemSusChem, 13 (7). pp. 1793-1799. ISSN 1864-5631

https://doi.org/10.1002/cssc.201903543

This is the peer reviewed version of the following article: P. Zheng, J. Su, Y. Wang, W. Zhou, J. Song, Q. Su, N. Reeves-McLaren, S. Guo, ChemSusChem 2020, 13, 1793, which has been published in final form at https://doi.org/10.1002/cssc.201903543. This article may be used for non-commercial purposes in accordance with Wiley Terms and Conditions for Use of Self-Archived Versions.

Reuse
Items deposited in White Rose Research Online are protected by copyright, with all rights reserved unless indicated otherwise. They may be downloaded and/or printed for private study, or other acts as permitted by national copyright laws. The publisher or other rights holders may allow further reproduction and re-use of the full text version. This is indicated by the licence information on the White Rose Research Online record for the item.

Takedown
If you consider content in White Rose Research Online to be in breach of UK law, please notify us by emailing eprints@whiterose.ac.uk including the URL of the record and the reason for the withdrawal request.

eprints@whiterose.ac.uk
https://eprints.whiterose.ac.uk/

A high-performance primary nanosheet heterojunction cathode composed of $Na_{0.44}MnO_2$ tunnels and layered $Na_2Mn_3O_7$ for Na-ion batteries

Peng Zheng,[*a] Jiaxin Su,[a] Yibing Wang,[a] Wei Zhou,[a] Jiajia Song, [a] Qinmei Su,[a] Nik Reeves-McLaren,[b] and Shouwu Guo,[c]

[a] School of Materials Science and Engineering, Shaanxi University of Science and Technology, Xian 710021, Shaanxi, P. R. China.

[b] Department of Materials Science and Engineering, University of Sheffield, Sheffield, S1 3JD, United Kingdom.

[c] Department of Electronic Engineering, School of Electronic Information and Electrical Engineering, Shanghai Jiao Tong University, Shanghai 200240, P. R. China

E-mail: zhengpeng@sust.edu.cn;

Abstract: Due to its large capacity and high average potential, the structure and reversible O-redox compensation mechanism of $Na_2Mn_3O_7$ have recently been analyzed. However, capacity fade and low coulombic efficiency following subsequent cycles have also been shown, which result from oxygen evolution at high charge voltages. Herein, a $Na_{0.44}MnO_2$•$Na_2Mn_3O_7$ heterojunction of primary nanosheets was prepared by a sol-gel-assisted high temperature sintering method. In the nanodomain regions, the close contact of $Na_{0.44}MnO_2$ not only supplies multidimensional channels to improve the rate performance of the composite, but also plays the role of pillars for enhancing the cycling stability and Coulombic efficiency; this is accomplished by suppressing oxygen evolution, which is confirmed by HRTEM, cyclic voltammetry and charge-discharge curves. As the cathode of a Na-ion battery, at 200 mA g^{-1} after 100 cycles, the $Na_{0.44}MnO_2$ •$Na_2Mn_3O_7$ heterojunction retains an 88 % capacity and the Coulombic efficiency approaches 100 % during the cycles. At 1000 mA g^{-1}, the $Na_{0.44}MnO_2$ •$Na_2Mn_3O_7$ heterojunction has a discharge capacity of 72 mAh g^{-1}. In addition, the average potential is as high as 2.7 V between a range of 1.5 and 4.6 V. The above good performances indicate that heterojunctions are an effective strategy for addressing oxygen evolution by disturbing the long-range order distribution of manganese vacancies in the Mn-O layer.

Keywords: $Na_{0.44}MnO_2$ •$Na_2Mn_3O_7$ heterojunction, cathode, oxygen evolution, Na-ion battery

Introduction

High energy density Na-ion batteries (NIBs) are a promising alternative to Li-ion batteries (LIBs), not only because of their wide distribution and the low cost of sodium salts but also because they can be used as large energy storage equipment for electric vehicles (EVs) and electric power grids.[1-4] Various cathodes have been investigated, including polyanionic compounds,[5] Prussian blue[6-8] and transition metal oxides[9]. Among them, Na-Mn-O-based cathodes have attracted intensive research attention because of their low cost, nontoxicity and high capacity.[10] Sodium manganese oxide (Na_xMnO_2, $0<x\leq1$) was first reported by Parant *et al.* in 1971, and various structures have since been presented with changes in the x value.[11] Generally, compounds with $0.22\leq x\leq0.44$ it have a full tunnel structure. When $0.44<x\leq0.66$, a mixture of tunnels and layered structures is formed. In addition, a fully layered structure forms as $0.66<x\leq1$.[12] The above rich structures endow the cathodes with special performance. The S-type tunnel structure of $Na_{0.44}MnO_2$ (referred to as $Na_4Mn_9O_{18}$) has a three-dimensional (3D) structure, which is favorable for Na-ion transfer, but the theoretical capacity is only 121 mAh g^{-1}.[13] The layered structured of $Na_{0.7}MnO_2$ has a large capacity of 200 mAh g^{-1}, but the Mn-O slab gliding and Na-ion/vacancy-ordering transitions occur during the sodiation/desodiation process, which deteriorate the structure and cycle stability.[14,15] Doping active (such as Fe, Ti, and Ni) or inactive (such as Li and Mg) cations is an effective strategy to improve the cycling stability.[16-18] However, the voltage ranges of these cations are usually below 4.2 V, which is not favorable for enhancing the energy density.

Recently, a triclinic structure of $Na_2Mn_3O_7$ (denoted as $Na_{4/7-x}[\square_{1/7}Mn_{6/7}]O_2$) has received intensive research attention because it can be charged to 4.7 V (the charge compensation of the high voltage range is realized by reversible oxygen-redox), and it has a large capacity (250 mAh g^{-1} at 1/20 C), which favors a high energy density. These pioneering works analyzed the intrinsic structure, charge compensation mechanism and low-voltage hysteresis.[19-23] In the structure, there is one out of seven Mn vacancies in the TM layer, oxygen displays a distorted P3-type stack, and Na^+ occupies both a distorted prism and octahedral sites. The reversible oxygen-redox for the Na-deficient cathode results from the reaction between the nonbonding 2p orbitals of the oxygen atoms and the nearby Mn vacancies, which contribute two charge plateaus in the high voltage region.[20] Compared with oxygen-redox from a noble metal-based cathode (Na_2IrO_3 and Na_2RuO_3), the low cost $Na_2Mn_3O_7$ cathode is much more attractive.[24,25] However, capacity fading and a low Coulombic efficiency (C. E.) during cycles are still showed in these reports. For example, an 85 % capacity was reserved after 20 cycles from ref. [19], and a 50 % capacity was reserved after 50 cycles from ref. [22]. In addition, the C. E. is approximately 80 % for all subsequent cycles.[12-15] Because zero-strain and immobility of the Mn-ion features are exhibited by this material, the abovementioned shortcomings are the result of oxygen evolution during the high voltage range charge.[13] Thus, the stability of multi O-redox processes and the cycle stability of the $Na_2Mn_3O_7$ cathode need to be enhanced.

Herein, we report a $Na_{0.44}MnO_2$•$Na_2Mn_3O_7$ heterojunction of primary nanosheets prepared by a sol-gel-assisted high temperature sintering method. The $Na_{0.44}MnO_2$ and

$Na_2Mn_3O_7$ phases are randomly distributed on one nanosheet and are in close contact. The nanosheets were then linked with each other to form a lamellar structure. The tunnel structure of $Na_{0.44}MnO_2$ not only favors Na-ion transfer to improve the rate capability, but also plays the role of pillars for suppressing long-range structural evolution induced by O-redox processes, especially at high voltages. The above description is confirmed by the overlapping cyclic voltammetry (CV) curves at high voltages showing a nearly 100 % C. E. during 100 cycles. Thus, the $Na_{0.44}MnO_2$ •$Na_2Mn_3O_7$ heterojunction (named NMO) exhibits good rate and cycling stability performance as a cathode for NIBs. Between the voltage range of 1.5 and 4.6 V, at 20 mA g^{-1}, the initial discharge capacity is as high as 278 mAh g^{-1}. At 200 mA g^{-1}, after 100 cycles, 88 % capacity is still retained. At 1000 mA g^{-1}, NMO has a discharge capacity of 72 mAh g^{-1}. In addition, the average potential of NMO is as high as 2.7 V.

Experimental

Materials Preparation

For the synthesis of the $Na_{0.44}MnO_2$ and $Na_2Mn_3O_7$ nanosheet heterojunction, in a typical process, manganese acetate (0.00784 mol) and sodium hydroxide at a mole ratio of 5:4 were dissolved in 5 ml deionized water under vigorous stirring. Then, the sol was heated in a domestic microwave oven (700 W) for 3 – 4 mins and sintered for 15 h at 750 °C. After naturally cooling to room temperature, the heterojunction was obtained. For the synthesis of bulk $Na_2Mn_3O_7$, the first step was to prepare $MnCO_3$ according to ref. 1. Then, stoichiometric amounts of $NaNO_3$ and $MnCO_3$ were mixed and heated at 600 °C for 4 h in a muffle furnace under an oxygen flow.

Materials characterization

X-ray diffraction (XRD) tests were performed on a Bruker D8 Advance diffractometer using Cu Kα radiation. Rietveld structure refinement was then analyzed using TOPAS software. X-ray photoelectron spectrometry (XPS) was conducted on a PHI 5000 VersaProbe III. The morphology was observed by field-emission scanning electron microscopy (FESEM, S-4800, Hitachi) and transmission electron microscopy (TEM, FEI Tecnai F20 microscope). A thermogravimetric (TG) analysis was conducted with a rate of 10 °C min^{-1} and using a Ta55 apparatus. The exact metal ion molar ratio of the sample was determined by inductive coupled plasma optical emission spectrometry (ICP−OES, Thermo 7000).

Electrochemical test.

Electrochemical measurements were conducted in a two-electrode coin cell (CR-2032), using NMO as the positive electrode and sodium metal foil as the negative electrode. The electrolyte was a 1 M $NaClO_4$ in 1:1 by volume ethylene carbonate (EC) and diethyl carbonate (DEC), and a Celgard 2500 membrane/glass fiber was used as the separator. The cells were assembled in an argon-filled glovebox (O_2, H_2O < 0.1 ppm). The cathodes were prepared by coating the slurry onto aluminum foil current collector. The slurry are composed of 80 wt % active material, 10 wt % acetylene black, and 10 wt % poly(vinylidene difluoride), and NMP was used as solvent. Subsequently, the materials were dried at 90 °C under vacuum for 10 h with active mass loading of ~2.5 mg cm^{-2}. A galvanostatic charge−discharge test was conducted on a Newaresles battery test system (BTS) (Shenzhen, China). Cyclic votammetric measurements were

carried out with the coin cells at a scan rate of 0.1 mV s^{-1} using a CHI 660e electrochemical workstation (ChenHua Instruments Co., China). Electrochemical impedance spectra (EIS) were recorded in the frequency range from 100 kHz to 10 mHz using a signal with an amplitude of 5 mV.

The apparent Li^+ diffusion coefficient (D_{Li}) could be calculated from the EIS profiles in the low-frequency zone by the following equations[39]:

$$Z_{re} = R_S + R_{ct} + \delta W^{-0.5} \quad (1\text{-}1)$$

$$\mathrm{D} = \frac{R^2T^2}{2S^2n^4\delta^2C^2F^4} \quad (1\text{-}2)$$

Here *R* is the gas constant, *T* is the absolute temperature, *S* is the surface area of the electrode (about 2 cm^2 here), *n* is the number of the electrons in the reactions, *F* is the Faraday constant, *C* is the concentration of Li^+ ions, δ is the Warburg factor, and W is the angular frequency in the low frequency region.

Results and discussion

The $Na_{0.44}MnO_2$•$Na_2Mn_3O_7$ heterojunction was synthesized through a sol-gel-assisted high temperature sintering method. The detailed procedure can be found in the experimental section. Figure 1 shows the phase and crystal structure of NMO. The peaks of NMO can be attributed to $Na_2Mn_3O_7$ (JCPDS 78-0193) and $Na_{0.44}MnO_2$ (JCPDS 27-0750), except for the small peak at $2\theta = 12.6^o$, which is indexed to crystal water (Figures 1a and S1a).[26] A Rietveld refinement plot was also generated (Figure S2); R_{wp} and R_p are 7.6 % and 5.6 %, respectively, and are located in a reasonable range, which indicates it is a high quality of Rietveld refinement. This finding suggests that the phase ratio of $Na_2Mn_3O_7$:$Na_{0.44}MnO_2$ is 69:31. $Na_2Mn_3O_7$ has a triclinic structure

with a $P\bar{1}$ space group, which can be described as a layered structure, as shown in Figure 1b.[23] The $[Mn_3O_7]^{2-}_{\infty}$ layers are made up of MnO_6 octahedra sharing an edge. NaO_5 and NaO_6 polyhedrals separate the sheets, and Na^+ occupies the other layer. Manganese vacancies lie in the $[Mn_3O_7]^{2-}_{\infty}$ layer, and oxygen lone pairs are close to the manganese vacancies, which are the original sites of reversible oxygen redox at high voltage.[19] $Na_{0.44}MnO_2$ has a tunnel structure with a $Pmc2_1$ space group and contains a 3D crystal structure composed of MnO_5 pyramids and MnO_6 octahedra (Figure 1b).[13] The open structure has large S tunnels and small tunnels, which favor Na^+ diffusion and accommodate the volume change during the (de)sodiation process.[27]

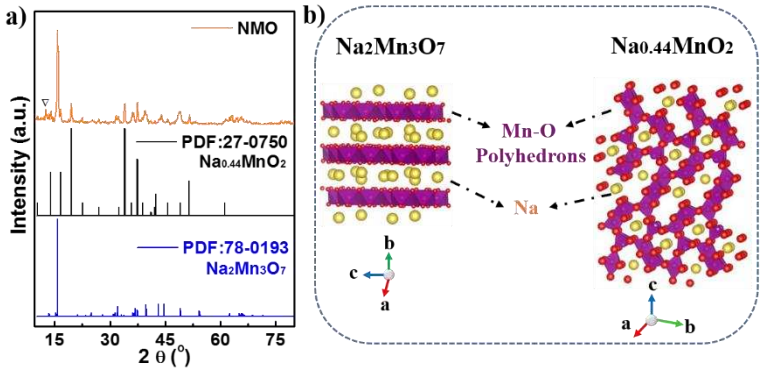

Figure 1. (a) XRD patterns of the $Na_{0.44}MnO_2$•$Na_2Mn_3O_7$ heterojunction, (b) crystal structure of the layered $Na_2Mn_3O_7$ and $Na_{0.44}MnO_2$ tunnels.

Lamellar NMO is composed of primary nanosheets, and small gaps can be observed between each nanosheet (Figure 2a). The gaps facilitate Na-ion transfer and can accommodate the lattice volume change of $Na_{0.44}MnO_2$. Figure 2b shows a TEM image, indicating that lamellar NMO is composed of several nanosheets. The thin nanosheets favor Na^+ diffusion and buffer the volume expansion and contraction during Na^+ insertion/extraction. Figure 2c shows a HRTEM image of NMO. Two phases distinctly

appear on one nanosheet. A lattice spacing of 0.55 nm is identified as the (-110) facet of $Na_2Mn_3O_7$, and the other lattice distance of 0.26 nm corresponds to the (350) facet of $Na_{0.44}MnO_2$. These two phases are closely connected, which verifies the formation of heterojunction structures in the nanodomain. To further verify these structures, additional images are provided. The large area of the (-110) $Na_2Mn_3O_7$ facet is shown in Figure 2d. In addition, Figure 2f displays the selected area electron diffraction (SAED) pattern from the zone axis in the [010] direction, which indicates that $Na_2Mn_3O_7$ is a single crystal structure. Figure 2e shows the HRTEM of $Na_{0.44}MnO_2$, and the tunnel structure is clearly observed. We consider the mole ratio of Na/ Mn in the sol-gel and the annealed temperature are the main factors for the formation of heterojunction. The Na: Mn mole ratio is 5: 4 in the sol-gel of the precursor, and the Na: Mn mole ratio in the NMO (750 ºC annealed product) is 4.4: 4 which is indicated by ICP analyze. These values are not consistent with the $Na_{0.44}MnO_2$ or $Na_2Mn_3O_7$ solely. As shown by the TG result (Figure S1a), almost no weight loss happened during 650 −750 ºC. As displayed by the XRD patterns (Figure S1b), as annealed at 650 ºC, $Na_2Mn_3O_7$ is the solely crystal in the sample. Combined with the Na/Mn ratio estimated from the ICP, there are some amorphous around the crystal. Up to 750 ºC, little $Na_{0.44}MnO_2$ crystal is appeared, may be this temperature is favor to transform the amorphous into $Na_{0.44}MnO_2$ crystal in this system.

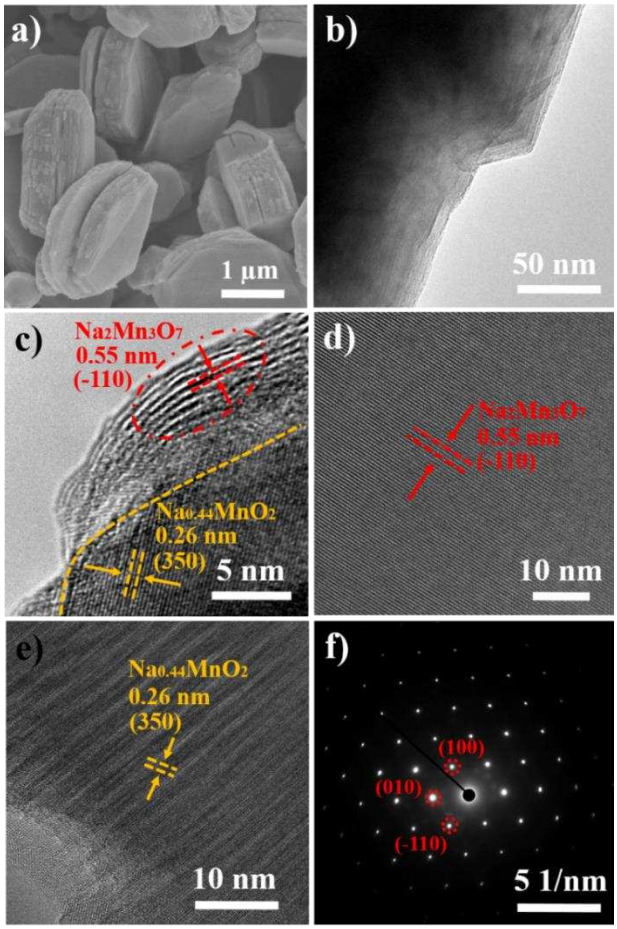

Figure 2. (a) SEM image, (b) TEM image, (c-e) HRTEM images, and (f) SEAD image of NMO.

The electrochemical performance of NMO as a cathode for NIBs was evaluated using coin-type half-cells with Na as the reference and counter electrode. Figure 3a displays the rate capabilities at 20, 50, 100, 200, 500, and 1000 mA g^{-1}, leading to discharge capacities as large as 278, 207, 163, 133, 98, and 72 mAh g^{-1}, respectively. When shifted to 200 mA g^{-1}, a capacity of 133 mAh g^{-1} is restored. Figure 3f shows the cycling stability at 200 mA g^{-1} after 100 cycles, with 89 % capacity (corresponding to 119 mAh g^{-1}) being retained. The initial Coulombic efficiency (C. E.) of the fresh cell is 61 %, and after several cycles, it can reach approximately 100 %. Table 1 shows the

electrochemical performance comparison of the Na-Mn-O cathodes. From the table, we can observe that our NMO has better stability and a better rate performance. Electrochemical impedance spectroscopy (EIS) (Figure 3b) measurements were conducted after various cycles. After the 2nd, 10th, 50th and 100th cycles, the semicircles in the high-frequency region are overlapped. The diameter of the semicircle represents the charge transfer resistance (R_{ct}), which is approximately 330 Ω .[28] The overlapped semicircles indicate the stable structure of the electrode. The inset image of Figure 3b is their fitted equivalent circuit. The low-frequency region represents sodium-ion diffusion. Figure 3c shows the corresponding Z_{re} vs $\omega^{-1/2}$ plots. Because the σ (Warburg impedance coefficient) values of these cycles are close to each other, the sodium-ion diffusion coefficients are close to each other.[27,29] After the 2nd cycle, the calculated sodium-ion diffusion coefficient (D_{Na}) is 1.95×10^{-12} cm^2 s^{-1}. This outstanding rate capability is attributed to the tunnel structure of $Na_{0.44}MnO_2$ and the large interspaces between each nanosheet in the lamellar structure. As the large-sized Na^+ reaches a nanosheet near the spacious interspace, Na ions easily diffuse into $Na_2Mn_3O_7$ due to the close contact between $Na_{0.44}MnO_2$ and $Na_2Mn_3O_7$ in the heterojunction structure and the rich 3D and 2D channels of $Na_{0.44}MnO_2$.

Figure 3d shows the galvanostatic charge−discharge profiles of fresh coin-type half-cells; the open-circuit voltage (OCV) is approximately 3.0 V. The profiles are stepwise profiles below 4.0 V, which result from the Na^+/vacancy ordering of $Na_{0.44}MnO_2$.[26] The capacity above 4.0 V accounts for 31% of the whole capacities. The average potential versus Na/Na^+ is 2.7 V. The multiphase transition processes of the stepwise profiles can

be reflected by the CV curves (Figure 3e). Multiple redox couples are observed below 4.0 V, which are attributed to the deintercalation/intercalation processes of $Na_{0.44}MnO_2$ and $Na_2Mn_3O_7$.[30] These couples can be expressed as $Na_{0.4}MnO_2 \leftrightarrow NaMnO_2$ and $Na_2Mn_3O_7 \leftrightarrow Na_4Mn_3O_7$.[19,31-32,38] For the 1st charge process, the sharp 4.2 and 4.6 V anodic peaks are attributed to $Na_2Mn_3O_7 \leftrightarrow NaMn_3O_7$ and charge compensation is executed by O-redox.[19] The 4.2 V peaks disappear in subsequent cycles, which is in accordance with the charge−discharge profiles.

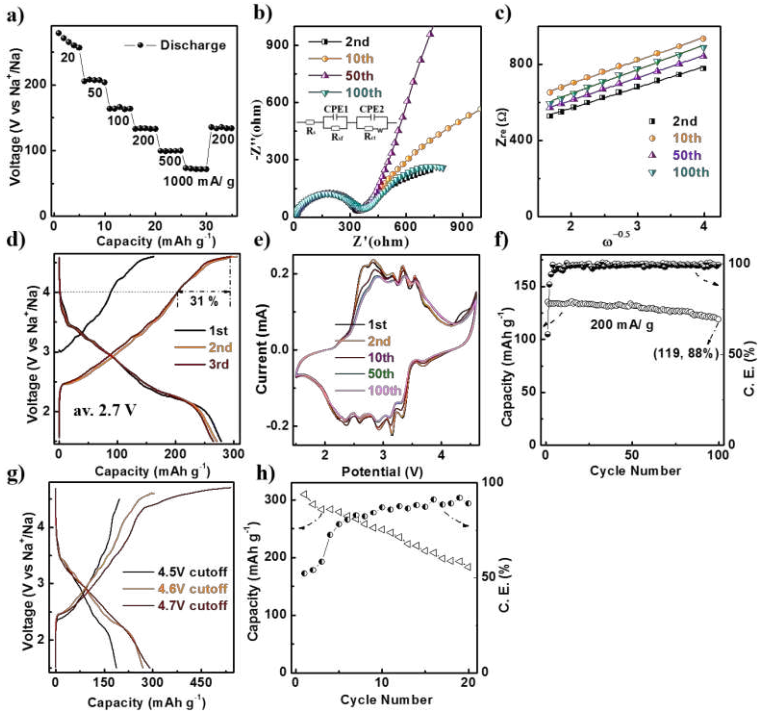

Figure 3. Electrochemical profiles of NMO: (a) rate capability, (b) Nyquist plots, (c) the relationship between low frequency and real resistance, (d) charge−discharge profiles at 20 mA g^{-1}, (e) cyclic voltammograms, (f) cycling stability at 100 mA g^{-1}, (g) 2nd charge−discharge profiles at various cutoff voltages, and (h) cycling stability at 20 mA g^{-1} between 1.5 and 4.7 V.

According to the report,[19] $Na_2Mn_3O_7$ can be charged to 4.7 V. Then, the NMO

electrodes were tested at various cutoff voltages (Figure 3g). The length order of the 4.5 V plateau region for the charge curve is 4.7 V cutoff > 4.6 V cutoff > 4.5 V cutoff for each 2nd cycle, and the discharge capacities are 291, 269 and 188 mAh g^{-1}, respectively. However, their C. E. show the reverse order, 54, 88 and 95 %, respectively. The lowest C. E. of the 4.7 V cutoff curve is the result of the large capacity loss at high voltage. The cycling stability with the 4.7 V cutoff is shown in Figure 3h, after 20 cycles, a 59 % capacity is retained. To explore the stability mechanism of NMO, we further analyzed the electrochemical performance of the $Na_2Mn_3O_7$ cathode.

Table 1. Comparison of the electrochemical performances of the various Na-Mn-O electrodes.

Cataode electrodes	**Potential range (V)**	**Average potential (V)**	**Capacity retention**	**Rate performance**	**References**
$Na_{0.4}MnO_2$	2.0-4.0		62 mAh g^{-1}/100th at 11.1 mA g^{-1}	79.3 mAh g^{-1} at 444 mA g^{-1}	ref. [33]
$Na_{0.44}MnO_2$	2.0-3.8		99 mAh g^{-1}/100th at 12.1 mA g^{-1}	82.8 mAh g^{-1} at 1000 mA g^{-1}	ref. [34]
F-$Na_{0.44}MnO_2$	2.0-4.2		115 mAh g^{-1}/150th at 121 mA g^{-1}	90 mAh g^{-1} at 600 mA g^{-1}	ref. [27]
$Na_{0.44}MnO_2$-$Na_{0.7}MnO_2$	1.5-4.3	2.72	119 mAh g^{-1} /100th at 200 mA g^{-1}	80.6 mAh g^{-1} at 1000 mA g^{-1}	ref.[35]
$Na_4Mn_2O_5$ •$Na_{0.7}MnO_2$	1.5-4.0	2.55	199 mAh g^{-1}/100th	142 mAh g^{-1} at	ref.[36]

			at 50 mA g^{-1}	1000 mA g^{-1}	
$NaMn_3O_5$	1.5-4.7	2.75	153 mAh g^{-1}/20th at 20 mA g^{-1}	115 mAh g^{-1} at 1000 mA g^{-1}	ref.[37]
$Na_2Mn_3O_7$	1.5-4.7		170 mAh g^{-1}/20th at 1/20 C		ref.[19]
$Na_2Mn_3O_7$	1.5-4.5	2.75	107 mAh g^{-1}/50th at 30 mA g^{-1}		ref.[22]
$NaCrO_2$	1.5-3.8		93.2 mAh g^{-1} / 1100th at 10 C	83.6 mAh g^{-1} at 50 C	ref.[40]
$Na_3V_2(PO_4)_3$	2.3-3.9		82 mAh g^{-1} / 2500th at 10 C	80.7 mAh g^{-1} at 50 C	ref.[41]
$Na_{0.44}MnO_2$ •$Na_2Mn_3O_7$	1.5-4.6	2.7	145 mAh g^{-1} /100th at 200 mA g^{-1}	72 mAh g^{-1} at 1000 mA g^{-1}	**This work**

Bulk $Na_2Mn_3O_7$ is synthesized by a solid-state reaction. In the XRD patterns (Figure 4a), all the peaks of the as-prepared sample can be indexed to the JCPDS 78-0193 card, which indicates that it is a pure $Na_2Mn_3O_7$ phase. Figure 4b shows the initial charge−discharge profiles with different cutoff voltages. Due to the existence of a large amount of long-range periodic manganese vacancies (one out of seven Mn are vacant in the Mn-O layer), two obvious potential plateaus appear at 4.2 and 4.5 V with cutoff curves of 4.6 and 4.7 V, respectively; the 4.5 V potential plateau is not obtained for the 4.5 V cutoff curve. The high voltage potential plateaus are ascribed to the shrinkage/expansion of manganese-site vacancies during the charge/discharge

process.[20] As suggested,[20,21] at the high voltage range, charge compensation is performed by O-redox (O^{2-} / $(O_2)^{n-}$, n = 4, 3, 2, 1 or 0). The higher the charge voltage, the more favorable it is to release oxygen gas (n = 0); thus, the 4.5 V potential plateaus are not stable and tend to release oxygen, as indicated by the initial C. E. of the various cutoff curves (Figure 3h and 4b). Among the curves, the 4.5 V cutoff curve shows the best cycling stability among the various cutoff curves. After 40 cycles, 83 % capacity is retained, but the C. E. of the following cycles are equal to 90 % (Figure 4c). Due to the zero-strain feature of $Na_2Mn_3O_7$, the fade-off capacities for the subsequent cycles are induced by oxygen gas release. The reduced capacities and released oxygen gas are also indicated by the shifting and reduced O-redox peaks in the CV curves with a 4.7 V cutoff (Figure 4d).

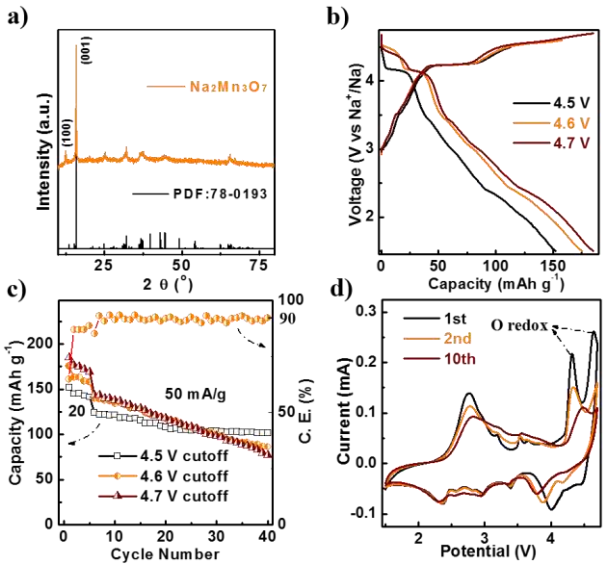

Figure 4. Electrochemical profiles of the as-synthesized $Na_2Mn_3O_7$ bulk: (a) XRD patterns, (b) initial charge−discharge profiles at various cutoffs, (c) cycling stability at various cutoffs, and (d) CV curves with a 4.7 V cutoff.

For $Na_2Mn_3O_7$, an increase in the long-range order distribution of Mn vacancies

indicates more accumulated stress due to manganese-site vacancy shrinkage/expansion; this makes it easy to release oxygen and leads to a low C. E and poor cycling stability. In the heterojunction, $Na_2Mn_3O_7$ is the main phase ($Na_2Mn_3O_7$:$Na_{0.44}MnO_2$ is 69:31), but its potential plateaus (4.2 and 4.5 V) are not obvious in the charge-discharge curves (Figure 3d and 3g). Thus, the long-range order distribution of manganese vacancies are disturbed by $Na_{0.44}MnO_2$, which is also indicated by the HRTEM image (Figure 2c). Combining these results with the nearly 100 % C. E. of the subsequent NMO cycles (Figure 3f), we speculate that the close contact of $Na_{0.44}MnO_2$ plays the role of a pillar to make the manganese vacancies display a short-range order distribution; thus, oxygen release is suppressed and a stable framework is retained. To verify the sturdy structure, after 100 cycles, the cell was dispatched. Figure 5a, b and c show the morphologies of the cycled electrode, which is still lamellar and composed of nanosheets. In addition to the O, Na, and Mn elements (Figure 5d), F is also uniformly distributed on the surface, which is the result of forming a cathode-electrolyte interface (CEI) layer. Although $Na_{0.44}MnO_2$ has a volume change during the cycle, due to the random distribution of $Na_{0.44}MnO_2$ and $Na_2Mn_3O_7$, the nanosheets can buffer the volume expansion and contraction even after long-term cycling, so the composite has good structural integrity.

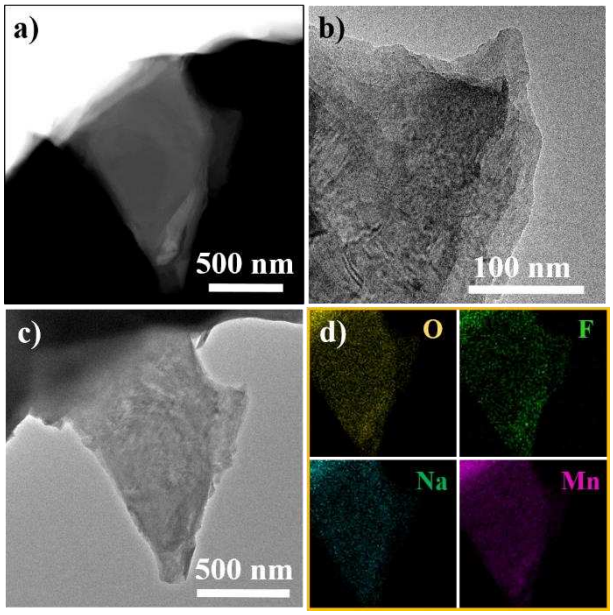

Figure 5. (a) STEM image, (b and c) TEM image, and (d) EDS mapping of the cycled NMO electrode.

To further explore the structural evolution of NMO during the desodiation/sodiation process, ex situ XRD was performed. As shown in Figure 6a, during (de)sodiation, the (-110) peak of $Na_2Mn_3O_7$ has negligible shifting, which is in accord with its zero-strain feature[21]. Except for the shifting of the (140) and (200) peaks of $Na_{0.44}MnO_2$, no new peak appears. During charging, the (140) and (200) peaks shift toward larger 2θ values, and as they discharge to 2.7 V, they move back and overlap with the original ones; this phenomenon is in line with the solid-solution behavior of $Na_{0.44}MnO_2$.[34] However, the shifting extent of the (200) peak is much smaller than that of the (140) peak, which may be the result of the interaction between $Na_2Mn_3O_7$ and $Na_{0.44}MnO_2$. These reversible structural evolutions induce good cycling stability. To verify the O-redox charge compensation mechanism of the NMO at the high voltage range, the ex situ O 2p XPS spectra are displayed in Figure 6b. After Gaussian fitting, in addition to the oxygenated

deposited species and lattice oxygen (529.5 eV) peaks, a new peak appears at 531 eV for charges of 4.2 and 4.6 V (termed C 4.2 V and C 4.6 V,), respectively, which can be attributed to peroxo-like species ($(O_2)^{n-}$)[22]. The O-redox charge compensation mechanism is confirmed at the high voltage regions for NMO, which is the same as $Na_2Mn_3O_7$. The Mn 2p XPS spectra of the NMO and Na_2Mn_3O could be seen Figure S3.[22]

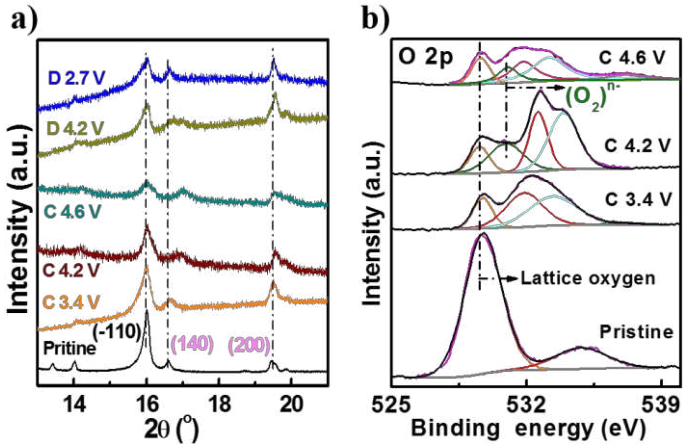

Figure 6. (a) Ex situ XRD patterns and (b) the ex situ O 2p XPS spectra of the NMO electrode at various charge/discharge depths.

Conclusions

In summary, a lamellar composite composed of $Na_{0.44}MnO_2$•$Na_2Mn_3O_7$ heterojunction was prepared by a sol-gel-assisted high temperature sintering method. Due to the pillar function of $Na_{0.44}MnO_2$, the heterojunction can enhance the low coulombic efficiency and poor cycling stability of $Na_2Mn_3O_7$. At 200 mA g^{-1}, a capacity of 88 % is still retained (corresponding to 119 mAh g^{-1}) after 100 cycles, and the Coulombic efficiency approaches 100 % during the cycles. The pillar function that contains the long-range order distribution of manganese vacancies in the Mn-O layer is disturbed by $Na_{0.44}MnO_2$ nanodomains, which is verified by HRTEM, CV curves and

charge−discharge profiles. The voids between the nanosheets of the lamellar and the tunnels of $Na_{0.44}MnO_2$ are favorable for improving the rate performance of the composite. At 1000 mA g^{-1}, the discharge capacity is as large as 72 mAh g^{-1}. The enhanced electrochemical performances of NMO indicate that the heterojunction structure is a valid strategy to address the shortcoming of $Na_2Mn_3O_7$.

Acknowledgements

The authors acknowledge the financial support from National Natural Science Foundation of China (No. 51702200).

References

[1] Liu, Q.; Hu, Z.; Chen, M.; Zou, C.; Jin, H.; Wang, S.; Chou, S.-L.; Dou, S.-X. *Small* **2019,** *15,* 1805381.

[2] Xia, H.; Zhu, X.; Liu, J.; Liu, Q.; Lan, S.; Zhang, Q.; Liu, X.; Seo, J. K.; Chen, T.; Gu, L.; Meng, Y. S. *Nature Communications* **2018,** *9,* 5100.

[3] Zhao, C.; Ding, F.; Lu, Y.; Chen, L.; Hu, Y.-S. *Angewandte Chemie International Edition* **2019,** DOI: 10.1002/ange.201912171.

[4] Sada, K.; Barpanda, P. *MRS Advances* **2019,** DOI: 10.1557/adv.2019.297.

[5] Zhou, W.; Xue, L.; Lü, X.; Gao, H.; Li, Y.; Xin, S.; Fu, G.; Cui, Z.; Zhu, Y.; Goodenough, J. B. *Nano Letters* **2016,** *16,* 7836-7841.

[6] Jiang, Y.; Yu, S.; Wang, B.; Li, Y.; Sun, W.; Lu, Y.; Yan, M.; Song, B.; Dou, S. *Advanced Functional Materials* **2016,** *26,* 5315-5321.

[7] Li, L.; Nie, P.; Chen, Y.; Wang, J. *Journal of Materials Chemistry A* **2019,** *7,* 12134-12144.

[8] Yue, Y.; Binder, A. J.; Guo, B.; Zhang, Z.; Qiao, Z.-A.; Tian, C.; Dai, S. *Angewandte Chemie International Edition* **2014,** *53,* 3134-3137.

[9] Wang, P.-F.; You, Y.; Yin, Y.-X.; Guo, Y.-G. *Advanced Energy Materials* **2018,** *8,* 1701912.

[10] Ortiz-Vitoriano, N.; Drewett, N. E.; Gonzalo, E.; Rojo, T. *Energy & Environmental Science* **2017,** *10,* 1051-1074.

[11] Parant, J.-P.; Olazcuaga, R.; Devalette, M.; Fouassier, C.; Hagenmuller, P. *Journal of Solid State Chemistry* **1971,** *3,* 1-11.

[12] Zhang, J.; Wang, W.; Wang, W.; Wang, S.; Li, B. *ACS Applied Materials & Interfaces* **2019,** *11,* 22051-22066.

[13] He, X.; Wang, J.; Qiu, B.; Paillard, E.; Ma, C.; Cao, X.; Liu, H.; Stan, M. C.; Liu, H.; Gallash, T.; Meng, Y. S.; Li, J. *Nano Energy* **2016,** *27,* 602-610.

[14] Kumakura, S.; Tahara, Y.; Kubota, K.; Chihara, K.; Komaba, S. *Angewandte Chemie International Edition* **2016,** *55,* 12760-12763.

[15] Nam, K. W.; Kim, S.; Yang, E.; Jung, Y.; Levi, E.; Aurbach, D.; Choi, J. W. *Chemistry of Materials* **2015,** *27,* 3721-3725.

[16] Sun, Y.; Guo, S.; Zhou, H. *Energy & Environmental Science* **2019,** *12,* 825-840.

[17] Zhou, D.; Huang, W.; Lv, X.; Zhao, F. *Journal of Power Sources* **2019,** *421,* 147-155.

[18] Rong, X.; Liu, J.; Hu, E.; Liu, Y.; Wang, Y.; Wu, J.; Yu, X.; Page, K.; Hu, Y.-S.; Yang, W.; Li, H.; Yang, X.-Q.; Chen, L.; Huang, X. *Joule* **2018,** *2,* 125-140.

[19] Mortemard de Boisse, B.; Nishimura, S.-i.; Watanabe, E.; Lander, L.; Tsuchimoto,

A.; Kikkawa, J.; Kobayashi, E.; Asakura, D.; Okubo, M.; Yamada, A. *Advanced Energy Materials* **2018,** *8,* 1800409.

[20] Song, B.; Tang, M.; Hu, E.; Borkiewicz, O. J.; Wiaderek, K. M.; Zhang, Y.; Phillip, N. D.; Liu, X.; Shadike, Z.; Li, C.; Song, L.; Hu, Y.-Y.; Chi, M.; Veith, G. M.; Yang, X.-Q.; Liu, J.; Nanda, J.; Page, K.; Huq, A. *Chemistry of Materials* **2019,** *31,* 3756-3765.

[21] Li, Y.; Wang, X.; Gao, Y.; Zhang, Q.; Tan, G.; Kong, Q.; Bak, S.; Lu, G.; Yang, X.-Q.; Gu, L.; Lu, J.; Amine, K.; Wang, Z.; Chen, L. *Advanced Energy Materials* **2019,** *9,* 1803087.

[22] Wang, Q.; Yang, W.; Kang, F.; Li, B. *Energy Storage Materials* **2018,** *14,* 361-366.

[23] Adamczyk, E.; Pralong, V. *Chemistry of Materials* **2017,** *29,* 4645-4648.

[24] Perez, A. J.; Jacquet, Q.; Batuk, D.; Iadecola, A.; Saubanère, M.; Rousse, G.; Larcher, D.; Vezin, H.; Doublet, M.-L.; Tarascon, J.-M. *Nature Energy* **2017,** *2,* 954-962.

[25] Mortemard de Boisse, B.; Liu, G.; Ma, J.; Nishimura, S.-i.; Chung, S.-C.; Kiuchi, H.; Harada, Y.; Kikkawa, J.; Kobayashi, Y.; Okubo, M.; Yamada, A. *Nature Communications* **2016,** *7,* 11397.

[26] Zhang, J.; Yu, D. Y. W. *Journal of Power Sources* **2018,** *391,* 106-112.

[27] Shi, W.-J.; Yan, Y.-W.; Chi, C.; Ma, X.-T.; Zhang, D.; Xu, S.-D.; Chen, L.; Wang, X.-M.; Liu, S.-B. *Journal of Power Sources* **2019,** *427,* 129-137.

[28] Cao, J.; Guo, S.; Yan, R.; Zhang, C.; Guo, J.; Zheng, P. *Journal of Alloys and Compounds* **2018,** *741,* 1-6.

[29] Gao, L.; Chen, S.; Zhang, L.; Yang, X. *Journal of Alloys and Compounds* **2019,** *782,* 81-88.

[30] Ta, A. T.; Nguyen, V. N.; Nguyen, T. T. O.; Le, H. C.; Le, D. T.; Dang, T. C.; Man, M. T.; Nguyen, S. H.; Pham, D. L. *Ceramics International* **2019,** *45,* 17023-17028.

[31] Cao, Y.; Xiao, L.; Wang, W.; Choi, D.; Nie, Z.; Yu, J.; Saraf, L. V.; Yang, Z.; Liu, J. *Advanced Materials* **2011,** *23,* 3155-3160.

[32] Meng, Q.; Li, G.; Yue, J.; Xu, Q.; Yin, Y.-X.; Guo, Y.-G. *ACS Applied Materials & Interfaces* **2019**, DOI: 10.1021/acsami.9b12086.

[33] Zhang, Y.; Liu, Z.; Deng, H.; Xie, J.; Xia, J.; Nie, S.; Liu, W.; Liu, L.; Wang, X. *ChemElectroChem* **2019,** *6,* 1711-1721.

[34] Liu, Q.; Hu, Z.; Chen, M.; Gu, Q.; Dou, Y.; Sun, Z.; Chou, S.; Dou, S. X. *ACS Applied Materials & Interfaces* **2017,** *9,* 3644-3652.

[35] Xiao, Y.; Wang, P.-F.; Yin, Y.-X.; Zhu, Y.-F.; Yang, X.; Zhang, X.-D.; Wang, Y.; Guo, X.-D.; Zhong, B.-H.; Guo, Y.-G. *Advanced Energy Materials* **2018,** *8,* 1800492.

[36] Wang, X.; Wang, C.; Han, K.; Niu, C.; Meng, J.; Hu, P.; Xu, X.; Wang, Z.; Li, Q.; Han, C.; Huang, Y.; Mai, L. *Advanced Energy Materials* **2018,** *8,* 1802180.

[37] Guo, S.; Yu, H.; Jian, Z.; Liu, P.; Zhu, Y.; Guo, X.; Chen, M.; Ishida, M.; Zhou, H. *ChemSusChem* **2014**, 7, 2115.

[38] Zheng, P.; Liu, T.; Su, Y.; Yuan, X.; Zhang, L.; Guo, S. *Journal of Alloys and Compounds* **2017**,703, 10-12.

[39] Mou, J.; Deng, Y.; He, L.; Zheng, Q.; Jiang, N.; Lin, D. *Electrochimica Acta* **2018**, 260, 101-111.

[40] Xi, K.; Chu, S.; Zhang, X.; Zhang, X.; Zhang, H.; Xu, H.; Bian, J.; Fang, T.; Guo, S.; Liu, P.; Chen, M.; Zhou, H. *Nano Energy* **2019**, 67, 104215.

[41] Li, W.; Yao, Z.; Zhou, C.-a.; Wang, X.; Xia, X.; Gu, C.; Tu, J. *Small* **2019**, 15, 1902432.